Hierarchical Software-Defined Control Architecture with MPC-Based Power Module to Interface Renewable Sources and Motor Drives

Liwei Zhou, *Member, IEEE*, Matthias Preindl, *Senior Member, IEEE*

***Abstract*—A hierarchical control architecture is designed with model predictive control (MPC)-based power module for generalized renewable applications including single/three-phase grid, solar, battery, electric motor, etc. The hierarchical control architecture is composed of three layers: (1) Central control layer for mode recognition of different types of interfaced load/source, reconstruction of power converter topologies, high level current/voltage/power control, generating references for local power module control and grid services for utility support; (2) Local module control layer for implementing MPC algorithm to track references from central controller with improved dynamic performance, stabilizing common-mode voltage, collecting ADC samplings and generate PWM signals for local power switches; (3) Application layer for the interface with different types of renewable loads/sources including single/three-phase grid, solar, battery, electric motor and so on. The merits of the designed control architecture include: (1) the reconfigurability to be suitable for different types of applications; (2) all non-isolated topologies with common-mode noise attenuation capability for renewable energy interfaces; (3) improved dynamic performance by local MPC power module; (4) high accuracy and robustness of the multi-layer MPC-based control without being influenced by the parametric modeling error from various interfaced applications; (5) grid services for abnormal condition utility support. The experimental results verified the proposed hierarchical control architecture.**

***Index Terms*—Hierarchical control, model predictive control, grid connection, motor drive, common-mode noise attenuation, renewable energy, grid services.**

I. Introduction

In practice, high performance power conversion systems require specialized design to satisfy the demands from various loads or sources especially with more renewable energy interfaces. Based on the features of different interfaced applications, the corresponding power control algorithms, parametric modeling and operating robustness design might be varying [1]–[3]. Also, the hardware circuitry topologies need specific design procedures. The repetitive power electronics design routines increase the cost both from software algorithm and hardware circuit perspectives [4]–[8]. Typically, a hardware-in-the-loop simulation system named Real Time Digital Simulator (RTDS) has been developed to combine the software algorithms with physical devices for the real-time validation. RTDS is a desired option to reduce the repetitive designing cost for the power electronics networks with the corresponding control algorithms at the holistic design stage. Furthermore, in the specific hardware and software design stages, a more detailed and practical strategy is needed for the power electronics to be interfaced with various applications. To provide more generalized power electronics design with less cost on redundant design procedures, the following three aspects can be considered as references. Firstly, modular concept is option to standardize the hardware components of the power electronics system. Especially for the renewable energy system with various types of interfaced applications, a basic power module can be designed to formulate different converter topologies for satisfying various demands. However, the existing modular power electronics either focus on micro-grid system level to redistribute the energy among different interfaced renewable energy sources or hardware device level to reconstruct different circuits within a certain application case [9]–[11]. Correspondingly, the specific converter design is unavoidable for each of the application. Secondly, to manipulate the power modules, multi-layer management structure has been typically applied for the digital control system. Similarly, the commonly used multi-layer management architectures are concentrating on either the whole micro-grid system level to manage among the distributed energy resources (DER) or individual converter level with cascaded control strategies for certain DER control purpose [12]–[14]. Thirdly, the generalized power module needs a robust and stable power control technique to satisfy different application requirements especially when interfaced with various renewable energy resources [15], [16]. Typical power electronics control techniques mainly include hysteresis control, linear control, sliding mode control, predictive control and artificial intelligent control. Among the various control techniques, hysteresis control is nonlinear which is difficult to model [17]. The linear method of PID control is simple for implementation [18]. However, the dynamic performance and resonant oscillation in high order filter system could cause operating issues under various types of energy interfaces. Sliding mode controller is configured to deal with the variable structured systems with different working modes [19]. Artificial intelligent methods such as fuzzy logic and neural network, can deal with complicated systems [20], [21]. But the interpretability and transparency need further studies. MPC is an advanced control technique which has good transient performance in the applications of power electronics voltage/current control [22]–[24].

To achieve the aforementioned three aspects for the generalization of power electronics system, a software-defined concept can be leveraged for the holistic system management. The software-defined idea has been proposed in several other areas such as mobile network, optical network, wireless sensor

network, data center, Internet of Things (IoT) or smart grid systems [25]–[36]. In which, [31] researched the software-defined mobile system with joint resource allocation and admission control mechanism. [30], [33] studied the secure distributed control and the detailed literature review of software-defined optical network. [27], [34] focused on the development of software-defined wireless sensor network with the specific control algorithms. [35] designed the resource allocation techniques for software-defined data center. [28] developed the traffic control strategies for software-defined IoT with machine learning tools. [25], [26], [29] studied the software-defined power systems with the focuses on communication, resilience against attacks and fault diagnosis, respectively. However, none of the software-defined researches covered the power electronics due to the application-oriented characteristic. The requirements of different power converters are typically varying and specific based on the interfaced applications and voltage/current ratings. Thus, the generalization of power electronics system needs to be software-defined with modular concept and hierarchical control architecture.

This paper proposes a hierarchical software-defined control architecture with MPC-based power modules to improve the performance of renewable energy conversion system with reconfigurability for different applications including single/three-phase grid, solar, battery, electric motor, etc. Firstly, the control architecture is introduced with the system modeling of local MPC-based power module and three types of interfaced applications. Secondly, the three-layer hierarchical control architecture is illustrated in details including central control layer, local module control layer and application layer. Thirdly, the merits of the developed control architecture are summarized with the corresponding experimental validations.

II. System Modeling

The proposed hierarchical control architecture is shown in Fig. 1. The architecture is composed of three layers which make the system reconfigurable for different types of load/source and power converter topologies. From top to bottom of Fig. 1, the multi-layer control architecture is constituted by central control layer, local module control layer and application layer. Specifically, the central control layer includes software-defined functions that are responsible for the recognition of different types of interfaced load/source, reconstruction of power converter with desired number of local modules, high level current/voltage/power/speed/torque control, generate references for local power module control, leakage current control for renewable energy interfaces and grid services for utility support. The local module control layer is composed of desired number of MPC-based power module unit as is shown in Fig. 2. The local power module is configured with MPC to improve the dynamic performance and attenuate the common-mode noise. The application layer defines the interface with different types of load/source including single/three-phase grid, battery, solar, motor, etc. This section analyzes the system modeling of the key basic component (local power module) and the correspondingly formulated different applications of the proposed hierarchical control architecture.

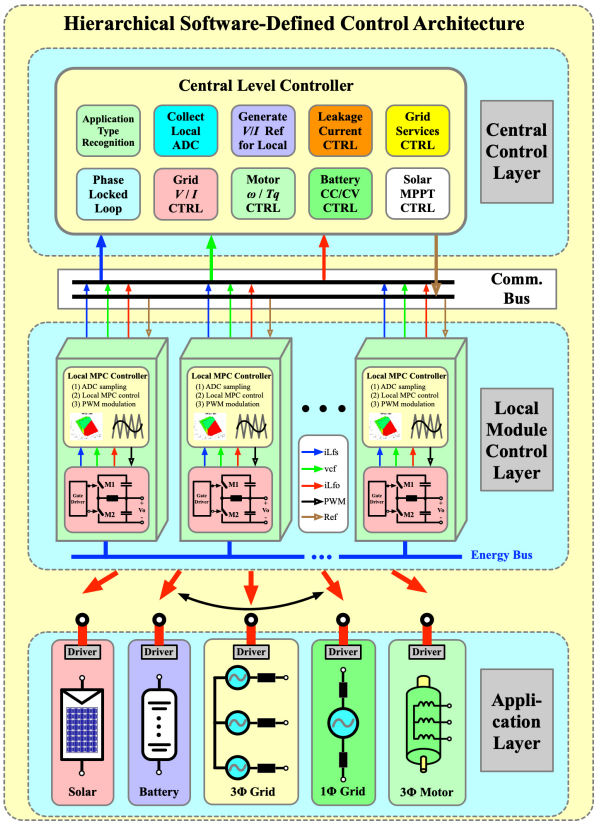

Fig. 1. Hirarchical control architecture with MPC-based power module.

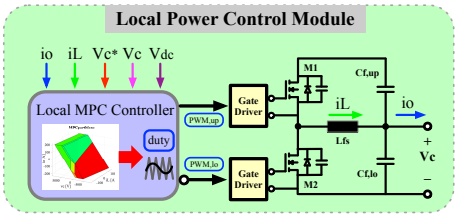

Fig. 2. Local MPC-based power module.

A. Local Power Module Modeling

As is shown in Fig. 2, the local power module consists of the upper/lower switches, switch side inductor, upper/lower output capacitors and the high-resolution MPC controller for the per module LC control. The differential equations for the local power module LC filter can be expressed as:

$$\dot{i}_{Lfs}(t) = -\frac{1}{L_{fs}} u_{Cf}(t) + \frac{v_{dc}}{L_{fs}} d(t) \tag{1a}$$

$$\dot{u}_{Cf}(t) = \frac{1}{C_f} i_{Lf}(t) - \frac{1}{C_f} i_{Lfo}(t). \tag{1b}$$

where L_{fs} and C_f are the switch side inductor and capacitor, respectively. i_{Lfs}, v_{Cf} and i_{Lfo} are the switch side inductor current, capacitor voltage and output side current. The local MPC control algorithm is designed based on the per phase LC filter to track the reference commands from the central control layer.

B. Application Modeling

With the recognition and reconstruction of different types of load/source interfaces from the central control layer, different number of local power modules are connected with the corresponding system models to perform the specific power control algorithms. The various types of applications include single/three-phase grid connection, motor traction and battery/solar.

1) Single-Phase Grid: Firstly, two local power modules can be connected in parallel to formulate a single-phase full-bridge transformerless grid-connected inverter as is shown in Fig. 3(a). The state space equations in ab reference frame can be expressed as:

$$\dot{i}_{Lfs,ab} = \frac{1}{L_{fs}}\mathbf{I}_{1\phi}v_{x,ab} - \frac{1}{L_{fs}}\mathbf{I}_{1\phi}v_{Cf,ab} \tag{2a}$$

$$\dot{v}_{Cf,ab} = \frac{1}{C_f}\mathbf{I}_{1\phi}i_{Lfs,ab} - \frac{1}{C_f}\mathbf{I}_{1\phi}i_{Lfo,ab} \tag{2b}$$

$$\dot{i}_{Lfo,ab} = \frac{1}{L_{fo}}\mathbf{I}_{1\phi}v_{Cf,ab} - \frac{1}{L_{fg}}\mathbf{I}_{1\phi}v_{g,ab}, \tag{2c}$$

where L_{fs}, C_f and L_{fo} are the switch side inductor, capacitor and grid side inductor, respectively, for the LCL filter. $i_{Lfs,ab}$, $v_{Cf,ab}$, $i_{Lfo,ab}$ and $v_{x,ab}$ are the switch side inductor current, capacitor voltage, grid side current and grid voltage for the single-phase grid-connected system, respectively. $\mathbf{I}_{1\phi} \in \mathbb{R}^{2\times2}$ is the identity matrix for single-phase grid connection system.

Leveraging the Park and Clarke transformations, the state space equations can be converted to the $dq0$ reference frame for the central level control:

$$\dot{i}_{Lfs,dq0} = \frac{1}{L_{fs}}\mathbf{I}_{dq0}v_{x,dq0} - \frac{1}{L_{fs}}\mathbf{I}_{dq0}v_{Cf,dq0} - \omega\mathbf{S}i_{Lfs,dq0} \tag{3a}$$

$$\dot{v}_{Cf,dq0} = \frac{1}{C_f}\mathbf{I}_{dq0}i_{Lfs,dq0} - \frac{1}{C_f}\mathbf{I}_{dq0}i_{Lfo,dq0} - \omega\mathbf{S}v_{Cf,dq0} \tag{3b}$$

$$\dot{i}_{Lfo,dq0} = \frac{1}{L_{fo}}\mathbf{I}_{dq0}v_{Cf,dq0} - \frac{1}{L_{fo}}\mathbf{I}_{dq0}v_{g,dq0} - \omega\mathbf{S}i_{Lfo,dq0} \tag{3c}$$

where ω is the angular velocity of the grid in rad/s. $\mathbf{S}$ is the matrix, [0, -1, 0; 1, 0, 0; 0, 0, 0], for the coupling terms of single-phase grid-connection model. $\mathbf{I}_{dq0} \in \mathbb{R}^{3\times3}$ is the identity matrix for $dq0$ grid connection system.

Different from the conventional inverter topologies, the upper/lower output capacitors of the local MPC-based power module provide common-mode leakage current bypassing paths for the formulated single-phase grid-connected inverter as is shown in Fig. 4(a). The common-mode voltage of the single-phase topology can be derived as:

$$v_{cm,1\phi} = v_{Cf,0,1\phi} = \frac{v_{Cf,a} + v_{Cf,b}}{2}. \tag{4}$$

The leakage leakage current is typically excited by the high frequency fluctuation of the common-mode voltage to be injected into the grid through a parasitic capacitor, C_{para}. The leakage current is defined as:

$$i_{lkg,1\phi} = i_{Lfo,0,1\phi} = C_{para}\frac{dv_{Cf0,1\phi}}{dt}. \tag{5}$$

With two MPC-based power modules connected in parallel for single-phase grid-connected inverter in Fig. 3(a), the equivalent common-mode circuit in Fig. 4(a) demonstrates that the leakage current can be bypassed by the upper/lower output capacitors with the zero-sequence voltage MPC control. From the control perspective, the embedded local power module zero-sequence voltage MPC can stabilize the common-mode voltage, $v_{Cf,0,1\phi}$, to be constant as half of DC bus voltage. Then, according to (5), the leakage current flowing to the grid will be largely attenuated.

2) Three-Phase Grid: Secondly, three local power modules can be connected in parallel to formulate a three-phase transformerless grid-connected inverter as is shown in Fig. 3(b). The state space equations in abc reference frame is similar with equation (2) by substituting $i_{Lfs,ab}$, $v_{Cf,ab}$, $i_{Lfo,ab}$, $v_{x,ab}$ and $\mathbf{I}_{1\phi} \in \mathbb{R}^{2\times2}$ with $i_{Lfs,abc}$, $v_{Cf,abc}$, $i_{Lfo,abc}$ and $v_{x,abc}$ and $\mathbf{I}_{3\phi} \in \mathbb{R}^{3\times3}$ for the three-phase system.

Leveraging the Park and Clarke transformations, the state space equations of three-phase system can be converted to the $dq0$ reference frame for the central level control which are similar with equation (3) in the single-phase system.

Different from the conventional three-phase inverter topologies, the upper/lower output capacitors of the local MPC-based power module provide common-mode leakage current bypassing paths for the formulated three-phase grid-connected inverter as is shown in Fig. 4(b). The common-mode voltage and leakage current expressions are similar to equations (4) and (5) by transferring single-phase variables into three-phase system.

With three MPC-based power modules connected in parallel for three-phase grid-connected inverter in Fig. 3(b), the equivalent common-mode circuit in Fig. 4(b) demonstrates that the leakage current can be bypassed by the upper/lower output capacitors with the zero-sequence voltage MPC control. From the control perspective, the embedded local power module zero-sequence voltage MPC can stabilize the common-mode voltage, $v_{Cf0,3\phi}$, to be constant as half of DC bus voltage. Then, the leakage current flowing to the grid will also be largely attenuated.

3) Motor Drive: Thirdly, three local power modules can also be connected in parallel to formulate a three-phase transformerless motor traction inverter as is shown in Fig. 3(c). Different from the grid-connected inverter applications, the motor drive interface does not require the grid side inductors, L_{fg}. Three power modules can be directly connected to the motor. Thus, the motor drive modeling can be separated into switch side LC filter modeling and PMSM modeling.

For the switch side LC filter modeling, the state space equations in abc reference frame can be derived as:

$$\dot{i}_{Lfs,abc} = \frac{1}{L_{fs}}\mathbf{I}_{3\phi}v_{x,abc} - \frac{1}{L_{fs}}\mathbf{I}_{3\phi}v_{Cf,abc} \tag{6a}$$

$$\dot{v}_{Cf,abc} = \frac{1}{C_f}\mathbf{I}_{3\phi}i_{Lfs,abc} - \frac{1}{C_f}\mathbf{I}_{3\phi}i_{motor,abc} \tag{6b}$$

where $i_{motor,abc}$ is the current flowing into the motor winding. Leveraging the Park and Clarke transformations, the state space equations can be converted to the $dq0$ reference frame for the central level control:

$$\dot{i}_{Lfs,dq0} = \frac{1}{L_{fs}}\mathbf{I}_{dq0}v_{x,dq0} - \frac{1}{L_{fs}}\mathbf{I}_{dq0}v_{Cf,dq0} - \omega\mathbf{M}i_{Lfs,dq0} \quad (7a)$$

$$\dot{v}_{Cf,dq0} = \frac{1}{C_f}\mathbf{I}_{dq0}i_{Lfs,dq0} - \frac{1}{C_f}\mathbf{I}_{dq0}i_{motor,dq0} - \omega\mathbf{M}v_{Cf,dq0} \quad (7b)$$

where $\mathbf{M}$ is the matrix, [0, -1, 0; 1, 0, 0; 0, 0, 0], for the coupling terms of motor drive model.

For the motor side modeling, a typical PMSM is analyzed in this section [37]. Different from the grid side inductor current, $i_{Lfg,dq0}$, the motor windng current, $i_{motor,dq0}$, can be modeled as:

$$\dot{i}_{motor,d} = \frac{1}{L_d}\left(v_{Cf,d} - R_s i_{motor,d} + \omega_e L_q i_{motor,q}\right) \quad (8a)$$

$$\dot{i}_{motor,q} = \frac{1}{L_q}\left(v_{Cf,q} - R_s i_{motor,q} - \omega_e\left(L_d i_{motor,d} + \psi\right)\right) \quad (8b)$$

$$T_e = \frac{3}{2}p\left(\lambda i_{motor,q} + \left(L_d - L_q\right)i_{motor,d}i_{motor,q}\right) \quad (8c)$$

$$\dot{\omega}_e = \frac{1}{J}\left(-B\omega_e + pT_e - pT_l\right) \quad (8d)$$

where L_d, L_q represent the dq component inductance of the motor, respectively; R_s is the stator winding resistance. ψ is the flux of the permanent magnets. ω_e is the electrical angular velocity of the rotor which is related to the mechanical angular velocity ω_m by the pole pairs p_p by $\omega_e = p_p\omega_m$. T_e and T_l are the electrical and load torques, respectively. B and J are the friction and inertia coefficients, respectively.

The motor bearing current and shaft voltage caused by the switching pulsation of the traction inverter is a key factor that could result in electric motor failure. The upper/lower output capacitors of the local MPC-based power module can provide common-mode leakage current bypassing paths for the formulated motor traction inverter as is shown in Fig. 4(c). The common-mode voltage of the motor traction inverter topology which is highly related to the shaft voltage of the motor can be derived as:

$$v_{cm,motor} = v_{Cf,0,motor} = \frac{v_{Cf,a} + v_{Cf,b} + v_{Cf,c}}{3}. \quad (9)$$

For the motor system, the leakage current is also typically generated by the high frequency fluctuation of the common-mode voltage to be injected into the motor bearing through the parasitic capacitor, C_{para}. The equivalent parasitic circuit model for the motor system has been displayed in Fig. 4(c) which consists of two paths. The first parasitic path is from the stator windings to the frame of the motor, C_{w2f}. The second path includes two cascaded sections which are from the stator windings to the rotor, C_{w2r}, and then from the rotor to the frame, $C_{r2f}, C_{b,NDE}, C_{b,DE}$. The leakage current, $i_{lkg,motor}$, generated by the high frequency fluctuation of the common mode voltage mainly flows through the first path of stator windings to the frame capacitor, C_{w2f}, because of its low impedance. And the second path of leakage current is mostly relevant to the bearing current and bearing voltage which are also generated by the high frequency fluctuation of common mode voltage. Specifically, C_{w2r}, C_{r2f}, $C_{b,NDE}$ and $C_{b,DE}$ are the stator windings to rotor capacitor, rotor

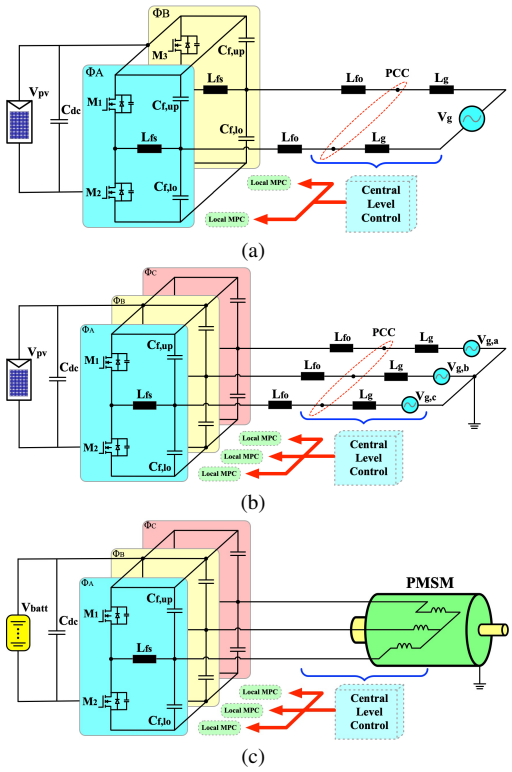

Fig. 3. (a) Single-phase grid (b) three-phase grid and (c) three-phase motor traction topological applications of the multi-layer control architecture.

to frame capacitor, non-drive end and drive end capacitors, respectively. So, the equivalent parasitic capacitance can be derived as:

$$C_{para} = \frac{(C_{r2f} + C_{b,NDE} + C_{b,DE})C_{w2r}}{(C_{r2f} + C_{b,NDE} + C_{b,DE}) + C_{w2r}} + C_{w2f}. \quad (10)$$

Thus, the leakage current also regarded as the bearing current is defined as:

$$i_{lkg,motor} = i_{0,motor} = C_{para}\frac{dv_{Cf,0,motor}}{dt}. \quad (11)$$

With three MPC-based power modules connected in parallel for the modified motor traction inverter in Fig. 3(c), the equivalent common-mode circuit in Fig. 4(c) demonstrates that the leakage current can be bypassed by the upper/lower output capacitors with the zero-sequence voltage MPC control. From the control perspective, the embedded local power module zero-sequence voltage MPC can stabilize the motor common-mode voltage, $v_{Cf0,motor}$, to be constant as half of DC bus voltage. Then, according to (11), the leakage current flowing to the motor bearing will also be largely attenuated.

III. Hierarchical Control Structure

The proposed hierarchical control structure is illustrated in this section. As is demonstrated in Fig. 1, the hierarchical control structure consists of three layers: (1) Central control layer for recognition of different types of load/source, reconfiguration of power converter topologies with desired number of power modules, high level current/voltage/power/speed/torque

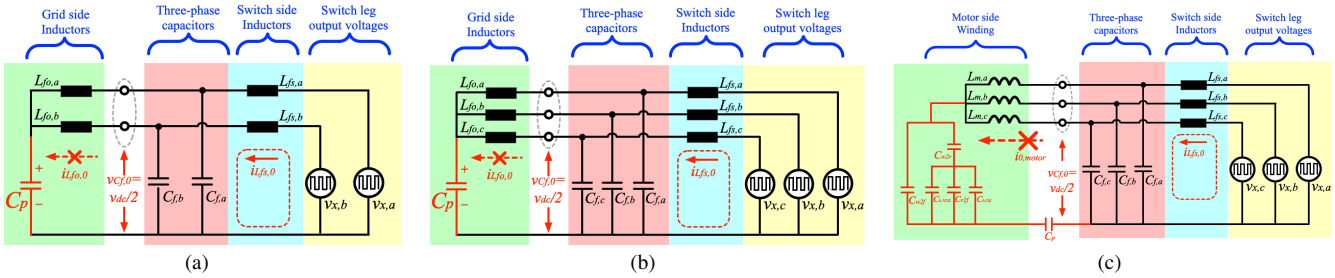

Fig. 4. Equivalent common-mode circuit of the formulated (a) Single-phase grid (b) three-phase grid and (c) three-phase motor inverters.

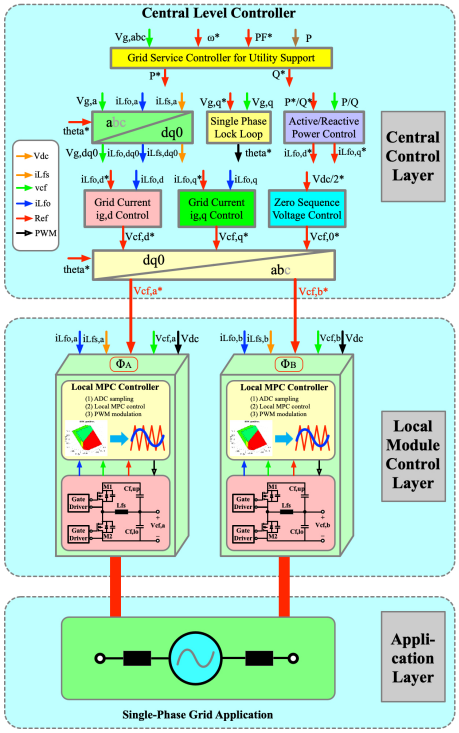

Fig. 5. Single-phase grid application of the hierarchical architecture.

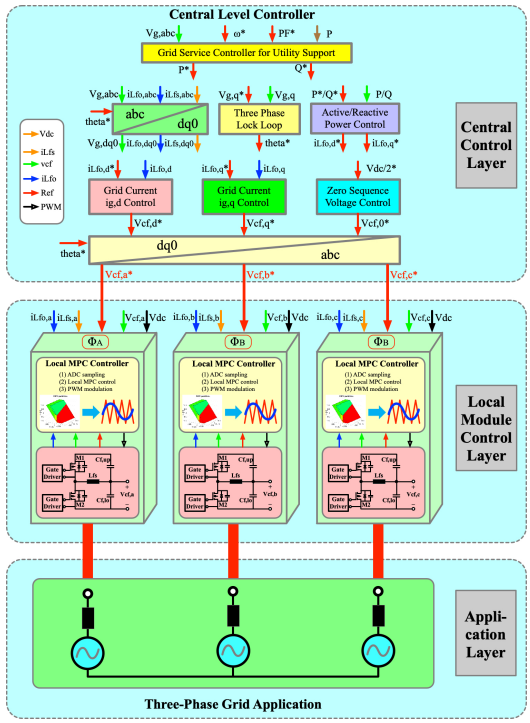

Fig. 6. Three-phase grid application of the hierarchical architecture.

control, generate references for local MPC-based power module control, leakage current control for renewable energy interfaces and grid services for utility support; (2) Local module control layer for implementing the MPC algorithm to track the references from the central controller with improved dynamic performance, stabilizing the common-mode voltage, collecting ADC samplings and generating PWM signals for local power switches; (3) Application layer for the interface with different types of load/source including single/three-phase grid, battery, motor drive and so on. Three typical interfaced applications of the proposed MPC-based hierarchical control architecture are demonstrated in this section including single-phase grid-connection, three-phase grid-connection and motor traction with the corresponding diagrams in Fig. 5, 6 and 7, respectively.

A. Single-Phase Grid Interface Control

Fig. 5 displays the control architecture for the application of single-phase grid interface. The corresponding power converter topology is shown in Fig. 3(a).

1) Central Control Layer: The central control layer is functioned to recognize the single-phase grid interface and reconfigure the power converter topology with two local power modules in parallel as is shown in Fig. 3(a). The specific functions of single-phase grid interface central control layer are illustrated as follows.

Firstly, the single-phase grid side inductor current, $i_{Lfo,ab}$, and output capacitor voltage, $v_{Cf,ab}$, are received from the local power modules and transformed into $dq0$ reference frame as $i_{Lfo,dq0}$ and $v_{Cf,dq0}$, respectively, for the high level control purpose.

Secondly, the single-phase phase-lock loop (PLL) is designed in the central control layer as is shown in Fig. 8(a). The virtual $\alpha\beta$ components of output capacitor voltage are constructed and transformed to dq axis to control the q component to be zero for the generation of accurate grid angular speed, ω, and phase angle, θ.

Thirdly, the grid service control functions are configured to provide active/reactive power compensations based on the

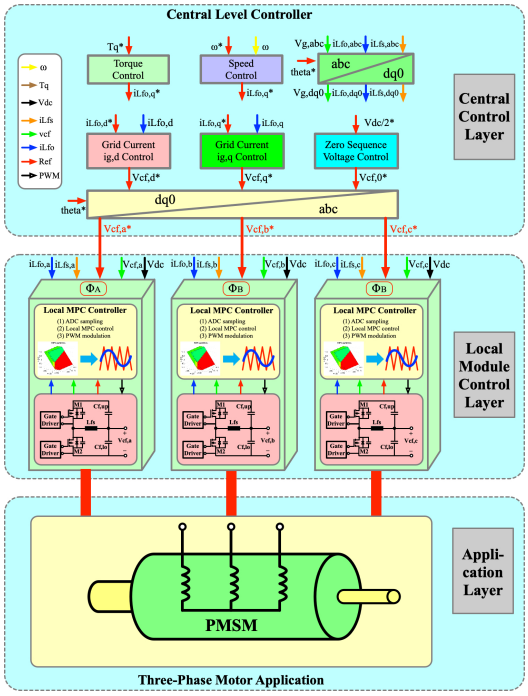

Fig. 7. Motor drive application of the hierarchical architecture.

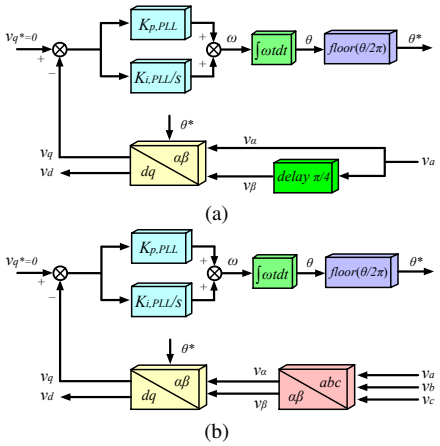

Fig. 8. (a) Single-phase and (b) three-phase PLL control blocks.

grid frequency/voltage abnormal conditions. The grid service control blocks are detailed in Fig. 9 by following the standardized principles of IEEE 1547 [38]. The general implementing methodology is to output the certain amount of active/reactive power for the distributed energy resources (DER) by following the prescribed linear curve functions. The linear functions in the grid service standards regulate the output active/reactive power based on the variations of grid voltage/frequency and output active power to compensate for the abnormal grid conditions. Six typical working modes of the grid services have been shown in Fig. 9 including constant reactive power mode (Const-Var), constant power factor mode (Const-PF), grid voltage and reactive power mode (Volt-Var), active power and reactive power mode (P-Q), grid frequency and active power mode (Freq-Watt), grid voltage and active power mode (Volt-Watt). Thus, the grid service controller in the central

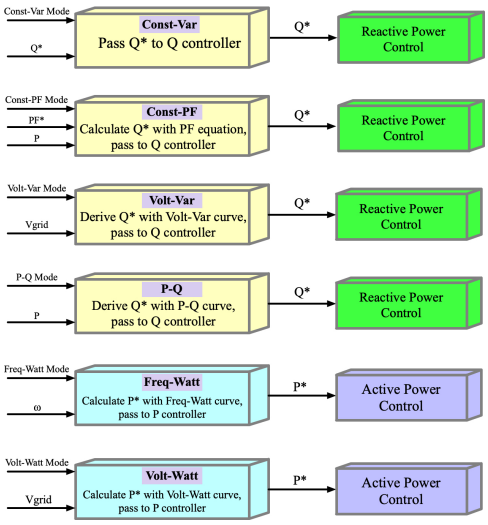

Fig. 9. Grid service control blocks in the central control for single/three-phase grid interfaced renewable energy applications.

control layer receives the measured grid voltage/frequency and active power of DER to generate the desired active/reactive power references, P^* and Q^*, for the active/reactive power controllers. The active/reactive power controllers derive the dq components of grid side inductor current references, $i^*_{Lfo,dq}$ for the following grid current dq controllers.

Fourthly, the grid side inductor current dq components, $i_{Lfo,dq}$, are controlled separately with two PI controllers to generate dq output capacitor voltage references, $v^*_{Cf,dq}$. And the zero-sequence output capacitor voltage reference, $v^*_{Cf,0}$, is configured as half of DC bus voltage, v_{dc}, to stabilize the common mode voltage. Combining the zero-sequence voltage control with the modified topology in Fig. 3(a), the leakage current can be attenuated from flowing into the grid. Then, the $dq0$ components of output capacitor voltage references are transformed into ab reference frame with the reversed Park and Clarke functions as, $v^*_{Cf,ab}$. The generated $v^*_{Cf,ab}$ then will be distributed to the per phase local module control layer as the tracking references of local MPC control.

2) Local Module Control Layer: The local module control layer of the single-phase grid interfaced system consists of two MPC-based power modules. Each of the power module is implementing the same MPC algorithm for the switch side LC filter to track the output capacitor voltage reference, $v^*_{Cf,ab}$, received from the central control layer.

For the MPC implementation, in every control period, the MPC controller receives the measured switch side inductor current, $i_{Lfs,abc}$, capacitor voltage, $v_{cf,abc}$, grid current, $i_{Lfo,abc}$, from ADC and capacitor voltage reference, $v^*_{cf,abc}$ from the grid current controller. An offline generated piecewise affine search tree is applied to derive the optimal duty cycle for the explicit MPC. The discrete state equations of switch side LC filter can be derived from the continuous equations in (1) as:

$$i_{Lfs}(k+1) = i_{Lfs}(k) - \frac{T_s}{L_{fs}} v_{Cf}(k) + \frac{v_{dc} T_s}{L_{fs}} d(k) \tag{12a}$$

$$v_{Cf}(k+1) = \frac{T_s}{C_f} i_{Lfs}(k) + v_{Cf}(k) - \frac{T_s}{C_f} i_{Lfo}(k). \tag{12b}$$

For the flexibility of implementing the explicit MPC and the convenience of experimentally adjusting the DC bus voltage during test, the last term of (12), $v_{dc}d(k)$, can be replaced by the phase leg output voltage, $v_x(k)$. The state-space model for MPC can be expressed in standard matrix format of

$$X_{k+1} = A_C X_k + B_C u_k + E_C e_k \tag{13}$$

where the variables and matrices for MPC control represent

$$A_C = \begin{bmatrix} 1 & -\frac{T_s}{L_{fs}} \\ \frac{T_s}{C_f} & 1 \end{bmatrix}, B_C = \begin{bmatrix} \frac{T_s}{L_{fs}} \\ 0 \end{bmatrix}, E_C = \begin{bmatrix} 0 \\ -\frac{T_s}{C_f} \end{bmatrix}, \tag{14a}$$

$$X_k = \begin{bmatrix} i_{Lfs}(k) \\ v_{Cf}(k) \end{bmatrix}, u_k = \begin{bmatrix} v_{dc} d(k) \end{bmatrix}, e_k = \begin{bmatrix} i_{Lfo}(k) \end{bmatrix}. \tag{14b}$$

In the MPC formulation, the inductor current/capacitor voltage references can be defined as $\bar{X}$ and the tracking errors between the measurement and the references are expressed as $\tilde{X}$ which are composed of

$$\bar{X}_k = \begin{bmatrix} i_{Lfs,ref}(k) \\ v_{Cf,ref}(k) \end{bmatrix}, \tilde{X}_k = \begin{bmatrix} i_{Lfs,ref}(k) - i_{Lfs}(k) \\ v_{Cf,ref}(k) - v_{Cf}(k) \end{bmatrix}. \tag{15}$$

Thus, the cost function includes two terms

$$min \ \sum_{k=0}^{N_c} \tilde{X}_k^T Q_C \tilde{X}_k + \sum_{k=0}^{N_p - 1} \triangle u_k^T R_C \triangle u_k. \tag{16}$$

For the penalties of the MPC cost function, Q_C and R_C represent the weighing factor matrices that are implemented on the state values and input values, respectively.

In MPC, the prediction horizon, H_p, is an essential factor to tune. H_p is correlated to the control period, T_s. Larger number of H_p can improve the performance of MPC such as accuracy, convergence. However, the computation burden will be increased accordingly since the MPC formulation array size will be expanded proportionally. Thus, the typical procedures to design H_p and T_s are: (1) choose a desired T_s based on the computational capability of micro-controller; (2) try H_p from low to high until the system is stable with desired transient response.

3) Application Layer: For the application layer, the interface between the local power modules and the single-phase grid are two grid side inductors, L_{fo}.

B. Three-Phase Grid Interface Control

Fig. 6 displays the control architecture for the application of three-phase grid interface. The corresponding power converter topology is shown in Fig. 3(b).

1) Central Control Layer: The central control layer is functioned to recognize the three-phase grid interface and reconfigure the power converter topology with three local power modules in parallel as is shown in Fig. 3(b). The specific functions of three-phase grid interface central control layer are illustrated as follows.

Firstly, the three-phase grid side inductor current, $i_{Lfo,abc}$, and output capacitor voltage, $v_{Cf,abc}$, are received from the local power modules and transformed into $dq0$ reference frame as $i_{Lfo,dq0}$ and $v_{Cf,dq0}$, respectively, for the high level control purpose.

Secondly, the three-phase PLL is designed in the central control layer as is shown in Fig. 8(b). The abc components of output capacitor voltage are received from local power modules and transformed to dq axis to control the q component to be zero for the generation of accurate grid angular speed, ω, and phase angle, θ.

Thirdly, the grid service control functions are configured to provide active/reactive power compensations based on the grid frequency/voltage abnormal conditions. The grid service control blocks are also following the working modes in Fig. 9 to generate the desired active/reactive power references, P^* and Q^*, for the active/reactive power controllers. The active/reactive power controllers derive the dq components of grid side inductor current references, $i^*_{Lfo,dq}$ for the following grid current dq controllers.

Fourthly, the grid side inductor current dq components, $i_{Lfo,dq0}$, are controlled separately with two PI controllers to generate dq output capacitor voltage references, $v^*_{Cf,dq}$. And the zero-sequence output capacitor voltage reference, $v^*_{Cf,0}$, is configured as half of DC bus voltage, v_{dc}, to stabilize the common mode voltage. Combining the zero-sequence voltage control with the modified topology in Fig. 3(b), the leakage current can be attenuated from flowing into the grid. Then, the $dq0$ components of output capacitor voltage references are transformed into abc reference frame with the reversed Park and Clarke functions as, $v^*_{Cf,abc}$. The generated $v^*_{Cf,abc}$ then will be distributed to the per phase local module control layer as the tracking references of local MPC control.

2) Local Module Control Layer: The local module control layer of the three-phase grid interfaced system consists of three MPC-based power modules. Each of the power module is implementing the same MPC algorithm for the switch side LC filter to track the output capacitor voltage reference, $v^*_{Cf,abc}$, received from the central control layer.

3) Application Layer: For the application layer, the interface between the local power modules and the three-phase grid are three grid side inductors, L_{fo}.

C. Motor Drive Interface Control

Fig. 7 illustrates the control architecture for the application of motor drive. The corresponding motor traction inverter topology is shown in Fig. 3(c). A permanent magnet synchronous motor (PMSM) is connected directly to the three local MPC-based power modules for the validation.

1) Central Control Layer: The central control layer is functioned to recognize the motor interface and reconfigure

the power converter topology with three local power modules in parallel as is shown in Fig. 3(c). The specific functions of motor interface central control layer are illustrated as follows.

Firstly, the rotor position is measured with a encoder board. And a speed controller is designed to control the rotor speed. The output of the speed controller is configured as the q component motor winding current reference, $i^*_{motor,q}$ to be cascaded with the following motor current controllers.

Secondly, the three-phase motor winding current, $i_{motor,abc}$, and output capacitor voltage, $v_{Cf,abc}$, are received from the local power modules and transformed into $dq0$ reference frame as $i_{motor,dq0}$ and $v_{Cf,dq0}$, respectively, for the high level control purpose.

Thirdly, the motor winding current dq components, $i_{motor,dq}$, are controlled separately with two PI controllers to generate dq output capacitor voltage references, $v^*_{Cf,dq}$. And the zero-sequence output capacitor voltage reference, $v^*_{Cf,0}$, is configured as half of DC bus voltage, v_{dc}. Then, the $dq0$ components of output capacitor voltage references are transformed into abc reference frame with the reversed Park and Clarke functions as, $v^*_{Cf,abc}$. The generated $v^*_{Cf,abc}$ then will be distributed to the per phase local module control layer as the tracking references of local MPC control.

2) Local Module Control Layer: The local module control layer of the motor interfaced system consists of three MPC-based power modules. Each of the power module is implementing the same MPC algorithm for the switch side LC filter to track the output capacitor voltage reference, $v^*_{Cf,abc}$, received from the central control layer.

3) Application Layer: For the application layer, the three local power modules are directly interfaced with the PMSM.

IV. Merits and Validations

The proposed hierarchical software-defined control architecture is validated experimentally on the MPC-based power module test bench with C3M0021120K MOSFETs and TMS320F280049 control card configured with CAN communication as is shown in Fig. 10. The merits of the designed architecture can be concluded in the following five aspects.

A. Reconfigurability with Unified Power Modules

Firstly, one of the major merits for the proposed hierarchical control architecture is the reconfigurability to be applied to different applications with the unified MPC-based power modules. As is shown in Fig. 1 and 10, different number of MPC-based power modules can be connected to formalize the desired circuitry topology and interfaced application. Fig. 11(a) and 11(b) show the single- and three-phase grid interfaced applications of the grid current, capacitor voltage, inductor current and DC voltage waveforms, respectively. The testing results of motor application are shown in Fig. 12(a) and 12(b) with speed step of 730 rpm and torque step of 26 Nm, respectively. The three applications, single/three-phase grid and motor, are all following the hierarchical control architectures illustrated in Fig. 5, 6 and 7, respectively. Besides the single-stage AC working modes of single/three-phase grid and motor traction applications, the proposed architecture can also be applied to the DC working mode and multi-stage energy conversion systems. Fig. 13(a) and 13(b) show the generalized cases of the software-defined architecture for DC/DC and two-stage DC/DC+DC/AC energy conversion systems. Specifically, one local power module can be configured for a holistic DC/DC converter or the DC/DC stage of the two-stage energy conversion system. Three power modules can be configured as the DC/AC stage for the two-stage system with a DC link capacitor in the middle. The corresponding validation results have been demonstrated in Fig. 14 with the output current, output voltage on both DC and AC working

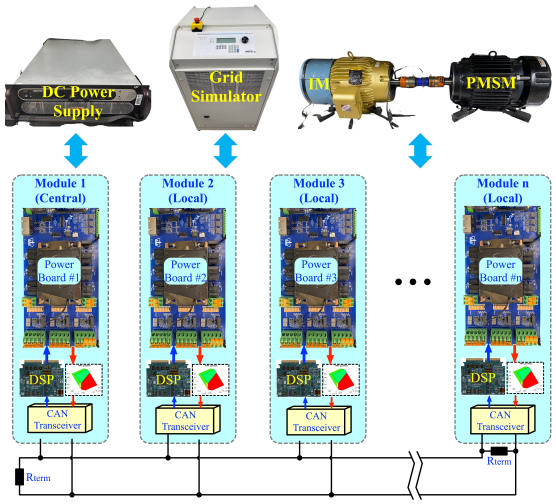

Fig. 10. Prototype of the hierarchical control structure.

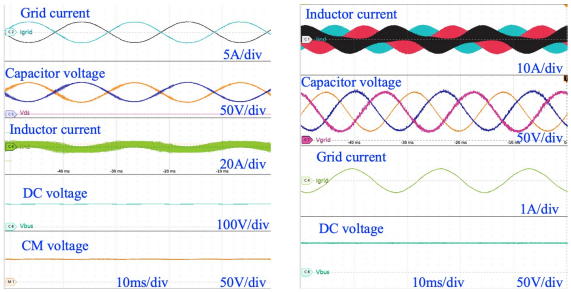

(a) (b)

Fig. 11. (a) Single-phase and (b) Three-phase grid interfaces grid current, capacitor voltage, inductor current and DC voltage steady state waveforms.

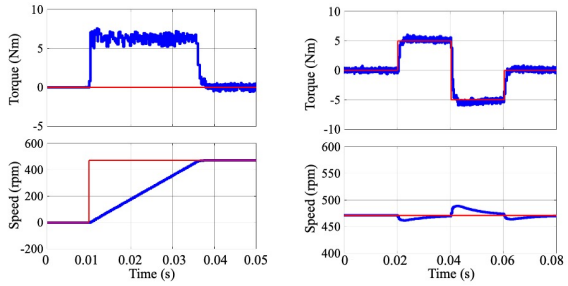

(a) (b)

Fig. 12. Captured ADC readings of motor (a) speed step from 0 to 470 rpm and (b) torque step from 5 to -5 Nm.

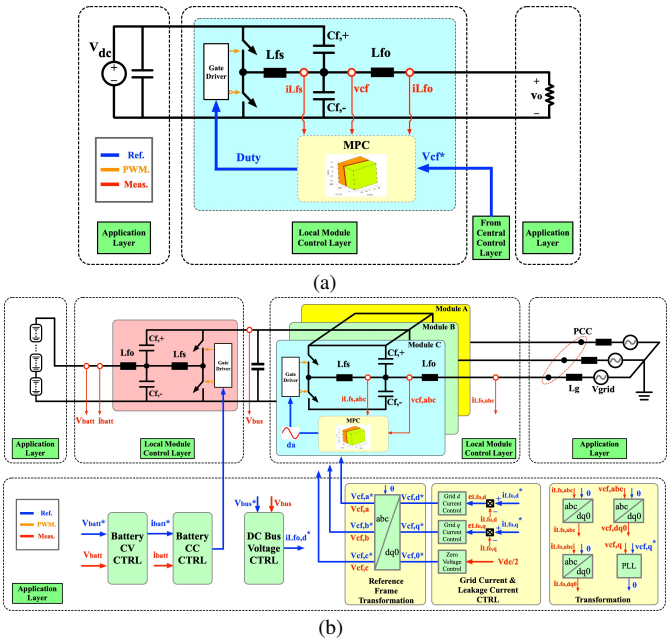

Fig. 13. Generalized cases of the software-defined architecture for (a) DC/DC and (b) two-stage DC/DC+DC/AC.

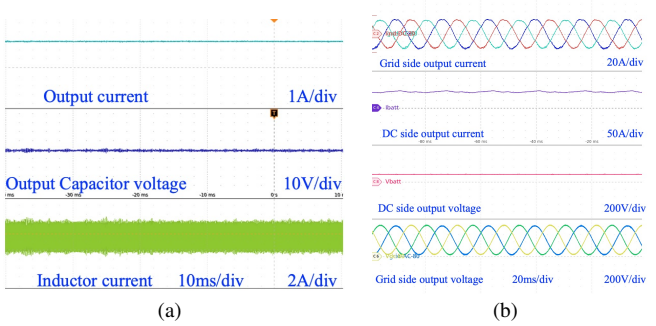

Fig. 14. Output current, output voltage waveforms for (a) DC/DC and (b) two-stage DC/DC+DC/AC energy conversion systems.

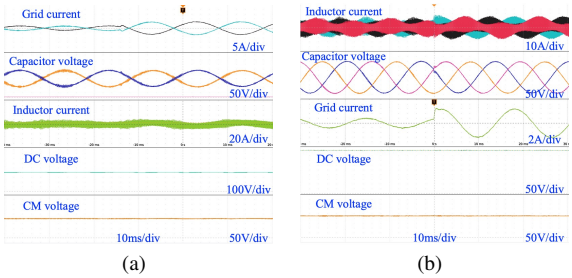

Fig. 15. (a) Single-phase and (b) Three-phase grid interfaces grid current, capacitor voltage, inductor current and DC voltage transient waveforms.

modes.

B. Improved Dynamic Performance with MPC-Based Local Layer Power Module

Secondly, the local level MPC control improves the dynamic performance by actively damping the resonance of the LCL filter and enabling a high control bandwidth. By inserting am

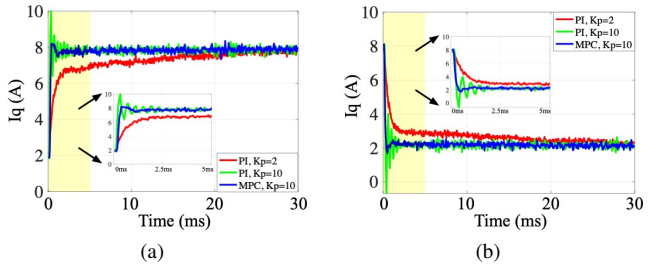

Fig. 16. Captured ADC readings of grid current steps from (a) 2A to 8A and (b) 8A to 2A for the proposed MPC and conventional PI methods.

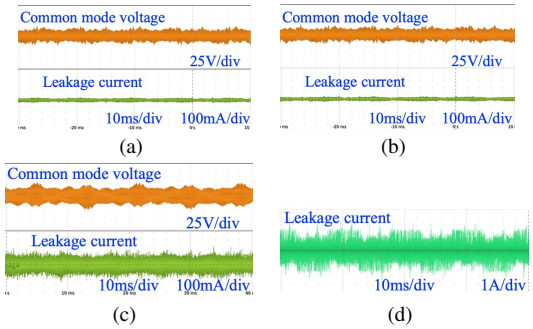

Fig. 17. The comparison of leakage current and common mode voltage for the (a) proposed single-phase grid connected topology with zero-sequence voltage control (b) proposed three-phase grid connected topology with zero-sequence voltage control (c) proposed three-phase grid connected topology without zero-sequence voltage control and (d) traditional topology without zero-sequence voltage control.

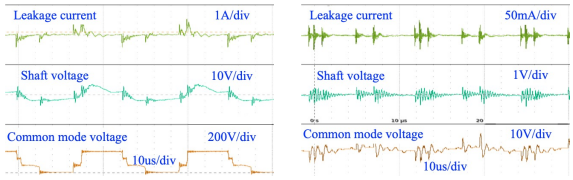

Fig. 18. The comparison of leakage current, shaft voltage and common mode voltage for the (a) conventional motor connected topology (b) proposed motor connected topology with zero-sequence voltage control.

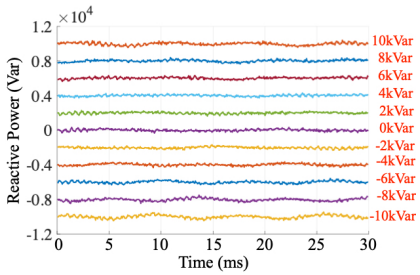

Fig. 19. Grid service results of Const-Var mode.

MPC loop between the central level output current PI and PWM modulation, the control gain is capable of being largely increased without inducing too much resonant oscillation. Fig. 15(a) and 11(b) shows the single- and three-phase grid interfaced applications of the grid current, capacitor voltage, inductor current and DC voltage waveforms, respectively, with

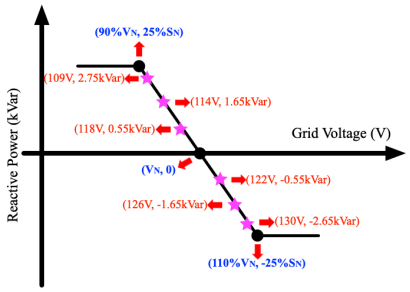

Fig. 20. Grid service results of Volt-Var mode.

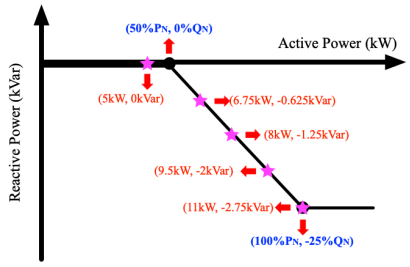

Fig. 21. Grid service results of P-Q mode.

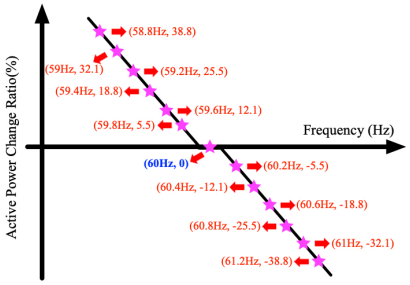

Fig. 22. Grid service results of Freq-Watt mode.

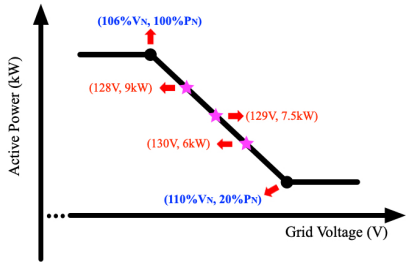

Fig. 23. Grid service results of Volt-Watt mode.

current step from 2A to 6A. Also, for a better comparison with the conventional PI control, three testing cases of the captured ADC readings for grid current from 2A to 8A and 8A to 2A are shown in Fig. 16(a) and 16(b), respectively. Compared with low K_p of the traditional PI, the proposed MPC control can track the reference 5 times faster without overshoot. Compared with high K_p of the traditional PI, the proposed MPC control performs more steadily without oscillation.

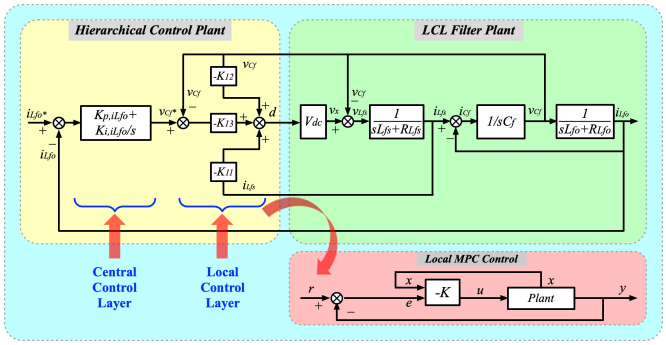

Fig. 24. The holistic modeling diagram of hierarchical control and plant model.

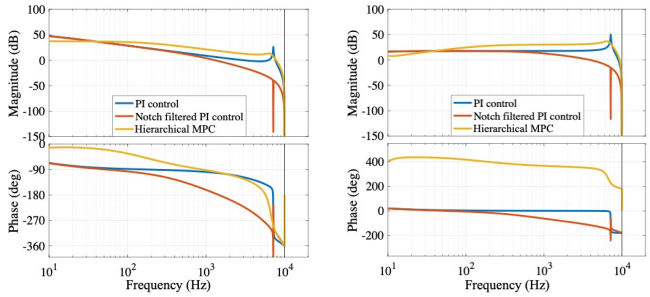

(a) (b)

Fig. 25. Comparison of bode plots for the control strategies of conventional PI, notch filtered PI and the proposed hierarchical MPC (a) from $i_{Lfo,err}$ to i_{Lfo} and (b) from $i_{Lfo,err}$ to v_{Cf}.

C. Non-Isolated Applications with Central Layer Zero-Sequence Control

Thirdly, the central layer manages a zero-sequence voltage control to be distributed to the local MPC power modules. With the zero-sequence controller combined with the modified topologies in Fig. 4(a), 4(b) and 4(c), the leakage current/common mode voltage of single/three-phase grid and shaft voltage/bearing current of motor can be attenuated. Thus, the non-isolated topology can save the cost of bulky transformer. Also, for the solar power interfaced energy conversion systems, the leakage current caused by the parasitic capacitance of the solar panels are non-negligible which could be suppressed by the developed topologies and control strategies. Specifically, Fig. 17(a)-17(d) compare the leakage current and common mode voltage for the modified single-phase grid-connected topology with zero-sequence controller, the modified three-phase grid-connected topology with zero-sequence controller, the modified grid-connected topology without zero-sequence controller and conventional grid-connected topology without zero-sequence controller, respectively. Only leveraging the modified topologies can reduce 2-3 times leakage current. However, combining the modified topologies with zero-sequence controller can reduce 10-15 times leakage current. Also, the comparison of leakage current, shaft voltage and common mode voltage for the conventional motor connected topology and proposed motor connected topology with zero-sequence voltage control in Fig. 18 demonstrates that the leak-

age current and shaft voltage on the motor can be attenuated by 10-20 times.

D. Robust MPC Free of Application Model Parameters Influence

Fourthly, for the proposed hierarchical control architecture, the control accuracy and robustness are guaranteed by the cascaded multi-layer control structure. As are shown in Fig. 5, 6 and 7 of the three applications, the output side inductor current is directly managed by the central layer controller and the corresponding output side inductance is free from the local MPC parametric modeling. Thus, the uncertainties of the equivalent output parameters caused by the various interfaced grid or motor will not influence the accuracy of the local MPC parametric modeling.

E. Grid Services for Abnormal Condition Utility Support

Lastly, for the grid interfaced renewable energy applications, the central layer of the proposed hierarchical control architecture can provide grid services for grid voltage/frequency abnormal condition utility support. The grid service control blocks in Fig. 9 have been validated through the proposed hierarchical control architectures with 120V grid and rated 11kVA DER. Five typical working modes of the grid services testing results have been shown in Fig. 19, 20, 21, 22 and 23 for the Const-Var, Volt-Var, P-Q, Freq-Watt and Volt-Watt modes, respectively. The grid service function algorithms are following the standardized piecewise linear curves to generate the desired active/reactive power based on the measured grid voltage/frequency or output active power values. Specifically, in the Const-Var mode of Fig. 19, 11 reactive power waveforms following the reference commands ranged from -10kVar to 10kVar are plotted by capturing the experimental readings. The Const-Var mode controller can generate accurate reactive power by tracking the references. In Fig. 20 of the Volt-Var mode curve, the piecewise linear curve is the standard requirement of reactive power for different grid voltages. Six grid voltage points varying from 109V to 130V are tested with the corresponding generated reactive power labeled in star. The Volt-Var controller can accurately follow the standard curve with the required reactive power under different grid voltage variations. In Fig. 21 of the P-Q mode, the piecewise linear curve is the standard requirement of reactive power for different active power outputs. Five active power output points varying from 5kW to 11kW are tested with the corresponding generated reactive power labeled in star. The P-Q controller can accurately follow the standard curve with the required reactive power under different active power output variations. In Fig. 22 of the Freq-Watt mode, the piecewise linear curve is the standard requirement of active power for different grid frequencies. Thirteen grid frequency points varying from 58.8Hz to 61.2Hz are tested with the corresponding generated active power change ratio values labeled in star. The Freq-Watt controller can accurately follow the standard curve with the required active power change ratio under different grid frequency variations. Lastly, in Fig. 23 of the Volt-Watt mode, the piecewise linear curve is the standard requirement of active power for different grid voltages. Three grid voltage points varying from 128V to 130V are tested with the corresponding generated active power values labeled in star. The Volt-Watt controller can accurately follow the standard curve with the required active power under different grid voltage variations.

F. Reliability of the Control

The reliability of the control performance is demonstrated in this subsection. For the proposed hierarchical control method, the corresponding control and system plant model has been shown in Fig. 24. The local level per phase switch side LC MPC is cascaded with the central level of grid side inductor current control. A linear-quadratic regulator (LQR) can be applied to derive the transfer function for the MPC algorithm portion in the control plant model of Fig. 24 to solve the cost function.

The typical LQR control diagram integrated with a dynamic system is shown in the bottom block of Fig. 24 where x, y, u, r represent the state variable, $[i_{Lfs}; v_{Cf}]$, output variable, i_{Lfs}, input variable of duty cycle, d, and tracking reference, $i_{Lfs,ref}$, respectively. The core algorithm of MPC to calculate the optimal duty cycle is a linear coefficient matrix, -**K**. And the MPC equation to calculate the optimal duty cycle based on the tracking error and state variable can be expressed as:

$$d = -\mathbf{K}\begin{bmatrix} i_{Lfs} \\ v_{Cf} \\ v_{Cf,err} \end{bmatrix} = -[K_{11}, K_{12}, K_{13}]\begin{bmatrix} i_{Lfs} \\ v_{Cf} \\ v_{Cf,err} \end{bmatrix} \tag{17}$$

where $v_{Cf,err}$ is the tracking error of the MPC calculated as $v_{Cf,ref} - v_{Cf}$.

Thus, the local level MPC can be expressed in the transfer function as Fig. 24. The transfer function from tracking error, $v_{Cf,err}$, to the measurement, v_{Cf}, of output capacitor voltage can be expressed as:

$$\begin{aligned} &G_{vCferr2vCf,MPC}(s) = \\ &\frac{-K_{13}G_{LCL,vx2iLfo}(s)(sL_{fo}+R_{Lfo})(sL_{fs}+R_{Lfs})/V_{dc}}{\{(sL_{fs}+R_{Lfs})+K_{11}[V_{dc}-G_{LCL,vx2iLfo}(s)(sL_{fo}+R_{Lfo})]/V_{dc}+} \\ &K_{12}G_{LCL,vx2iLfo}(s)(sL_{fs}+R_{Lfs})(sL_{fo}+R_{Lfo})/V_{dc}- \\ &K_{13}G_{LCL,vx2iLfo}(s)(sL_{fs}+R_{Lfs})(sL_{fo}+R_{Lfo})/V_{dc}\}. \end{aligned} \tag{18}$$

Furthermore, the transfer function from the reference, $v_{Cf,ref}$, to the measurement, v_{Cf}, of output capacitor voltage can be expressed as:

$$\begin{aligned} &G_{vCfref2vCf,MPC}(s) = \\ &G_{vCferr2vCf,MPC}(s)/[1+G_{vCferr2vCf,MPC}(s)]. \end{aligned} \tag{19}$$

Based on equation (19) and the LCL plant model in Fig. 24, the transfer function from the reference of output capacitor voltage, $v_{Cf,ref}$, to the measurement of grid side inductor current, i_{Lfo}, can be derived as:

$$\begin{aligned} &G_{vCfref2iLfo,MPC}(s) = \\ &G_{vCfref2vCf,MPC}(s)/(sL_{fo}+R_{Lfo}). \end{aligned} \tag{20}$$

Then, taking the central level grid side inductor current PI control into consideration, the cascaded MPC transfer function from tracking error, $i_{Lfo,err}$, to the measurement, i_{Lfo}, of grid side inductor current can be expressed as:

$$G_{iLfoerr2iLfo,MPC}(s) = G_{vCfref2iLfo,MPC}(s) \cdot G_{iLfo,PI}(s). \tag{21}$$

The hierarchical MPC transfer function from tracking error of grid side inductor, $i_{Lfo,err}$, to the measurement of output capacitor voltage, v_{Cf}, can be expressed as:

$$G_{iLfoerr2vCf,MPC}(s) = G_{vCfref2vCf,MPC}(s) \cdot G_{iLfo,PI}(s). \tag{22}$$

The resonance behavior and dynamic performance of the three control strategies for LCL filtered grid-connected inverter are analyzed based on the derived transfer functions. Fig. 25(a) and Fig. 25(b) show the bode plots comparison of transfer functions from the tracking error to the measurement of grid side inductor current and from the tracking error of grid side inductor current to the measurement of output capacitor voltage, respectively. The magnitude plots demonstrate that the conventional PI control has a convex spike at the resonant frequency point. The notch filtered PI control has a concave spike at the resonant frequency point. The developed hierarchical MPC attenuates the spike at the resonant frequency point and the control bandwidth is wider than the conventional PI, notch filtered PI and cascaded PI methods. The robustness and reliability are improved correspondingly.

G. Comparison with the Conventional Control

The proposed software-defined architecture is compared with the conventional methods to control the distributed energy resources. Firstly, for the hysteresis control of power converters, the extra work of linearization process and the need of accurate prediction for the hysteresis band require careful design procedures [17], [39]. Secondly, for the linear control techniques, the most commonly used method of PID is simple to implement [18]. However, the control parameters have noticeable influence on the steady state and dynamic performance which need to be tuned carefully. Especially, when the converter is configured as high order LC or LCL, the PID control may cause some resonance oscillation issues. Thirdly, for the predictive control methods, [40] developed an FCS-MPC method with observer and output side current sensors to deal with unbalanced conditions. [41] studied two types of FCS-MPC techniques for the reduction of both output side harmonics and the sensitivity to the distorted grid. [42] also developed the FCS-MPC strategies for the improvement of transient performance of grid-tied LCL converter based on $\alpha\beta$ frame. Fourthly, for the artificial intelligent control techniques, the fuzzy-logic-based method in [20] and the neural network method in [21] reconfigured the control mechanism with fuzzy logic rules and learning-based algorithms, respectively which are suitable for the highly nonlinear applications. The discretized power converters connected with the filters can be modeled with linearized state space equations. The explainable controllers are capable of dealing with such power conversion control process. The main differences of the proposed architecture can be summarized in three aspects: (1) The algorithm execution burden is relatively lower than the aforementioned MPC methods since the proposed method implements the algorithm for each phase LC instead of multi-phase topology with a holistic state space system. The MPC order is lower. The execution time is less than 4μs in every control interrupt. (2) The proposed architecture is configured with an MPC-based zero-sequence voltage control strategy to attenuate the leakage current with non-isolated topologies. Transformerless structure saves the cost on isolation. (3) The derived C code for per phase local MPC is smaller than 5KB which can be effortlessly stored in the DSP RAM.

H. Inductor and Capacitor Parametric Design

For the switch side inductor, the minimum inductance, $L_{fs,min}$, can be determined by the maximum required current ripple, $\Delta i_{Lfs,max}$, with the duty cycle of 0.5, d, switching frequency, f_{sw}, and DC bus voltage, V_{dc}

$$L_{fs,min} = \frac{d(1-d)V_{dc}}{f_{sw}\Delta i_{Lfs}}. \tag{23}$$

With the desired grid/switch side inductance determined, the capacitance can be designed by the minimum output voltage ripple, u_{ripple} and the resonant frequency of the LCL filter, ω_{res}. Specifically, the minimum capacitance is determined by the output voltage ripple which is expressed as

$$C_{f,up,min} + C_{f,lo,min} = \frac{1-d_{min}}{8L_{fs}u_{ripple}[\%]f_{sw}^2}. \tag{24}$$

Then, from the minimum available $C_{f,up,min}$ and $C_{f,lo,min}$, the value of capacitance can be adjusted to determine the resonant frequency of LCL filter system as is shown in

$$\omega_{res} = \sqrt{\frac{L_{fs}+L_{fo}}{L_{fs}L_{fo}(C_{f,up}+C_{f,lo})}}. \tag{25}$$

Based on (25), the capacitor values can be finally determined to choose a specific resonant frequency of the LCL filter. Then, with the help of ω_{res} and LCL parameters, the control bandwidth, ω_c, can be further designed to avoid the excitation.

There exist a trade-off between offline explicit MPC with less computation burden and the corresponding possible tracking error caused by the parameter variations. To explore the influences of LC filter parameters variations on the control behavior, the mismatch between the MPC state space parameters and the physical LC parameters is manually adjusted in Table I. Three sets of cases have been tested including: (1) varying only the switch side inductance, L_{fs}, mismatch; (2) varying only the output capacitance, C_f, mismatch; (3) varying both the switch side inductance, L_{fs}, and the output capacitance, C_f, mismatch. Based on the testing results, the variations of offline pre-selected L_{fs} and C_f can affect the accuracy of MPC tracking. Applying the variations on both L_{fs} and C_f can cause more error than only applying variations on either

L_{fs} or C_f. The largest possible error is 1.03% which occurs at a large mismatch of 60% on both L_{fs} and C_f.

For the influence of grid side inductance parameter on the control performance, since the local MPC is not leveraging this grid side inductance as the state space modeling, the per phase module of output capacitor voltage MPC tracking will not be affected by the variation of grid side inductance. The corresponding validation has been shown in Table II by manually adjusting the grid side inductance to check the influence on control performance. The tracking error is verified to be free from the variation of grid side inductance.

V. Conclusion

This paper develops a hierarchical software-defined control architecture with MPC-based power module to improve the performance of energy conversion system. The contributions can be summarized as: (1) a multi-layer structure is designed for generalized energy resource applications such as single/three-phase grid, motor and DC sources; (2) local MPC is configured for each power module to improve the dynamic performance and stability; (3) non-isolated topologies combined with zero-sequence MPC control save the cost of transformers. The experimental results validated the theoretical analysis.

References

[1] L. Subramanian, V. Debusschere, H. B. Gooi, and N. Hadjsaid, "A distributed model predictive control framework for grid-friendly distributed energy resources," *IEEE Transactions on Sustainable Energy*, vol. 12, no. 1, pp. 727–738, 2021.

[2] J. Choi, J.-I. Lee, I.-W. Lee, and S.-W. Cha, "Robust pv-bess scheduling for a grid with incentive for forecast accuracy," *IEEE Transactions on Sustainable Energy*, vol. 13, no. 1, pp. 567–578, 2022.

[3] G. Wang, G. Konstantinou, C. D. Townsend, J. Pou, S. Vazquez, G. D. Demetriades, and V. G. Agelidis, "A review of power electronics for grid connection of utility-scale battery energy storage systems," *IEEE Transactions on Sustainable Energy*, vol. 7, no. 4, pp. 1778–1790, 2016.

[4] A. Sharma, S. C. Srivastava, and S. Chakrabarti, "Testing and validation of power system dynamic state estimators using real time digital simulator (rtds)," *IEEE Transactions on Power Systems*, vol. 31, no. 3, pp. 2338–2347, 2016.

[5] B. Wang, X. Dong, Z. Bo, and A. Perks, "Rtds environment development of ultra-high-voltage power system and relay protection test," *IEEE Transactions on Power Delivery*, vol. 23, no. 2, pp. 618–623, 2008.

TABLE I
THE INFLUENCES OF SWITCH SIDE LC VARIATIONS ON MPC TRACKING.

L_{fs} Variation	Tracking Error	C_f Variation	Tracking Error	L_{fs}, C_f Variation	Tracking Error
60%	0.7%	60%	0.8%	60%	1.03%
40%	0.58%	40%	0.59%	40%	0.9%
20%	0.45%	20%	0.47%	20%	0.63%
0%	0.1%	0%	0.75%	0%	0.12%
-20%	-0.25%	-20%	-0.33%	-20%	-0.53%
-40%	-0.53	-40%	-0.63	-40%	-0.83%
-60%	N/A	-60%	N/A	-60%	N/A

TABLE II
THE INFLUENCES OF GRID SIDE L VARIATIONS ON MPC TRACKING.

Grid Side Inductance (μH)	4.5	18	45	180	450
Tracking Error (%)	0.25	0.21	0.18	0.14	0.12

[6] K. Ou, H. Rao, Z. Cai, H. Guo, X. Lin, L. Guan, T. Maguire, B. Warkentin, and Y. Chen, "Mmc-hvdc simulation and testing based on real-time digital simulator and physical control system," *IEEE Journal of Emerging and Selected Topics in Power Electronics*, vol. 2, no. 4, pp. 1109–1116, 2014.

[7] Z. Yang, Y. Wang, L. Xing, B. Yin, and J. Tao, "Relay protection simulation and testing of online setting value modification based on rtds," *IEEE Access*, vol. 8, pp. 4693–4699, 2020.

[8] Y. Zhang, H. Ding, and R. Kuffel, "Key techniques in real time digital simulation for closed-loop testing of hvdc systems," *CSEE Journal of Power and Energy Systems*, vol. 3, no. 2, pp. 125–130, 2017.

[9] M. Kim, A. Kwasinski, and V. Krishnamurthy, "A storage integrated modular power electronic interface for higher power distribution availability," *IEEE Transactions on Power Electronics*, vol. 30, no. 5, pp. 2645–2659, 2015.

[10] S. Kim and P. Enjeti, "A modular single-phase power-factor-correction scheme with a harmonic filtering function," *IEEE Transactions on Industrial Electronics*, vol. 50, no. 2, pp. 328–335, 2003.

[11] N. Pallo, T. Foulkes, T. Modeer, S. Coday, and R. Pilawa-Podgurski, "Power-dense multilevel inverter module using interleaved gan-based phases for electric aircraft propulsion," in *2018 IEEE Applied Power Electronics Conference and Exposition (APEC)*, 2018, pp. 1656–1661.

[12] Z. Li, C. Zang, P. Zeng, H. Yu, and S. Li, "Fully distributed hierarchical control of parallel grid-supporting inverters in islanded ac microgrids," *IEEE Transactions on Industrial Informatics*, vol. 14, no. 2, pp. 679–690, 2018.

[13] L. V. Bellinaso, H. H. Figueira, M. F. Basquera, R. P. Vieira, H. A. Gründling, and L. Michels, "Cascade control with adaptive voltage controller applied to photovoltaic boost converters," *IEEE Transactions on Industry Applications*, vol. 55, no. 2, pp. 1903–1912, 2019.

[14] J. He, Y. Liu, and Y. Wang, "Cascaded droop and inverse droop regulation for two-layer coordinated power flow control in series-connected power cells," *IEEE Transactions on Industrial Electronics*, vol. 68, no. 8, pp. 6939–6951, 2021.

[15] H. Alcahuaman, J. C. López, D. Dotta, M. J. Rider, and S. Ghiocel, "Optimized reactive power capability of wind power plants with tap-changing transformers," *IEEE Transactions on Sustainable Energy*, vol. 12, no. 4, pp. 1935–1946, 2021.

[16] M. Islam, N. Afrin, and S. Mekhilef, "Efficient single phase transformerless inverter for grid-tied pvg system with reactive power control," *IEEE Transactions on Sustainable Energy*, vol. 7, no. 3, pp. 1205–1215, 2016.

[17] Y. Wang, X. Ruan, Y. Leng, and Y. Li, "Hysteresis current control for multilevel converter in parallel-form switch-linear hybrid envelope tracking power supply," *IEEE Transactions on Power Electronics*, vol. 34, no. 2, pp. 1950–1959, 2019.

[18] J.-W. Jung, V. Q. Leu, T. D. Do, E.-K. Kim, and H. H. Choi, "Adaptive pid speed control design for permanent magnet synchronous motor drives," *IEEE Transactions on Power Electronics*, vol. 30, no. 2, pp. 900–908, 2015.

[19] L. Zheng, F. Jiang, J. Song, Y. Gao, and M. Tian, "A discrete-time repetitive sliding mode control for voltage source inverters," *IEEE Journal of Emerging and Selected Topics in Power Electronics*, vol. 6, no. 3, pp. 1553–1566, 2018.

[20] A. Bouafia, F. Krim, and J.-P. Gaubert, "Fuzzy-logic-based switching state selection for direct power control of three-phase pwm rectifier," *IEEE Transactions on Industrial Electronics*, vol. 56, no. 6, pp. 1984–1992, 2009.

[21] X. Fu and S. Li, "Control of single-phase grid-connected converters with lcl filters using recurrent neural network and conventional control methods," *IEEE Transactions on Power Electronics*, vol. 31, no. 7, pp. 5354–5364, 2016.

[22] C. Xue, L. Ding, H. Tian, and Y. Li, "Multi-rate Finite-Control-Set Model Predictive Control for High Switching Frequency Power Converters," *IEEE Transactions on Industrial Electronics*, vol. 0046, no. c, pp. 1–11, 2021.

[23] A. Bemporad, F. Borrelli, and M. Morari, "Model predictive control based on linear programming - The explicit solution," *IEEE Transactions on Automatic Control*, vol. 47, no. 12, pp. 1974–1985, 2002.

[24] R. Guzman, L. G. de Vicuña, A. Camacho, J. Miret, and J. M. Rey, "Receding-horizon model-predictive control for a three-phase vsi with an lcl filter," *IEEE Transactions on Industrial Electronics*, vol. 66, no. 9, pp. 6671–6680, 2019.

[25] M. H. Rehmani, A. Davy, B. Jennings, and C. Assi, "Software defined networks-based smart grid communication: A comprehensive survey," *IEEE Communications Surveys Tutorials*, vol. 21, no. 3, pp. 2637–2670, 2019.

[26] P. Danzi, M. Angjelichinoski, Stefanović, T. Dragičević, and P. Popovski, "Software-defined microgrid control for resilience against denial-of-service attacks," *IEEE Transactions on Smart Grid*, vol. 10, no. 5, pp. 5258–5268, 2019.

[27] R. Huang, Y. Dong, G. Bao, Y. Liu, M. Wei, J. Lu, and Y. Huo, "A new topology control algorithm in software defined wireless rechargeable sensor networks," *IEEE Access*, vol. 9, pp. 101 003–101 012, 2021.

[28] J. Yang, J. Zhang, and H. Wang, "Urban traffic control in software defined internet of things via a multi-agent deep reinforcement learning approach," *IEEE Transactions on Intelligent Transportation Systems*, vol. 22, no. 6, pp. 3742–3754, 2021.

[29] A. K. Al Mhdawi and H. S. Al-Raweshidy, "A smart optimization of fault diagnosis in electrical grid using distributed software-defined iot system," *IEEE Systems Journal*, vol. 14, no. 2, pp. 2780–2790, 2020.

[30] H. Yang, Y. Liang, Q. Yao, S. Guo, A. Yu, and J. Zhang, "Blockchain-based secure distributed control for software defined optical networking," *China Communications*, vol. 16, no. 6, pp. 42–54, 2019.

[31] G. Chen, Y. Zhang, Y. Shi, and Q. Zeng, "Joint resource allocation and admission control mechanism in software defined mobile networks," *China Communications*, vol. 16, no. 5, pp. 33–45, 2019.

[32] D. F. Macedo, D. Guedes, L. F. M. Vieira, M. A. M. Vieira, and M. Nogueira, "Programmable networks—from software-defined radio to software-defined networking," *IEEE Communications Surveys Tutorials*, vol. 17, no. 2, pp. 1102–1125, 2015.

[33] A. S. Thyagaturu, A. Mercian, M. P. McGarry, M. Reisslein, and W. Kellerer, "Software defined optical networks (sdons): A comprehensive survey," *IEEE Communications Surveys Tutorials*, vol. 18, no. 4, pp. 2738–2786, 2016.

[34] H. I. Kobo, A. M. Abu-Mahfouz, and G. P. Hancke, "Fragmentation-based distributed control system for software-defined wireless sensor networks," *IEEE Transactions on Industrial Informatics*, vol. 15, no. 2, pp. 901–910, 2019.

[35] M. Yang, H. Rastegarfar, and I. B. Djordjevic, "Physical-layer adaptive resource allocation in software-defined data center networks," *Journal of Optical Communications and Networking*, vol. 10, no. 12, pp. 1015–1026, 2018.

[36] D. Kreutz, F. M. V. Ramos, P. E. Veríssimo, C. E. Rothenberg, S. Azodolmolky, and S. Uhlig, "Software-defined networking: A comprehensive survey," *Proceedings of the IEEE*, vol. 103, no. 1, pp. 14–76, 2015.

[37] M. Preindl, "Robust control invariant sets and lyapunov-based mpc for ipm synchronous motor drives," *IEEE Transactions on Industrial Electronics*, vol. 63, no. 6, pp. 3925–3933, 2016.

[38] "Ieee application guide for ieee std 1547(tm), ieee standard for interconnecting distributed resources with electric power systems," *IEEE Std 1547.2-2008*, pp. 1–217, 2009.

[39] L. Malesani, P. Mattavelli, and P. Tomasin, "High-performance hysteresis modulation technique for active filters," *IEEE Transactions on Power Electronics*, vol. 12, no. 5, pp. 876–884, 1997.

[40] X. Chen, W. Wu, N. Gao, H. S.-H. Chung, M. Liserre, and F. Blaabjerg, "Finite control set model predictive control for lcl-filtered grid-tied inverter with minimum sensors," *IEEE Transactions on Industrial Electronics*, vol. 67, no. 12, pp. 9980–9990, 2020.

[41] P. Falkowski and A. Sikorski, "Finite control set model predictive control for grid-connected ac–dc converters with lcl filter," *IEEE Transactions on Industrial Electronics*, vol. 65, no. 4, pp. 2844–2852, 2018.

[42] T. Dragičević, "Model predictive control of power converters for robust and fast operation of ac microgrids," *IEEE Transactions on Power Electronics*, vol. 33, no. 7, pp. 6304–6317, 2018.